14

Compression of Spectral Images

Arto Kaarna
Lappeenranta University of Technology
Finland

1. Introduction

In this chapter we describe methods how to compress spectral imaging data. Normally the spectral data is presented as spectral images which can be considered as generalizations of colour images. Rapid technological development in spectral imaging devices has initiated the need for the compression of raw data. Spectral imaging has been central to many remote sensing applications like geology and environment monitoring. Nowadays, new application areas have arisen in industry, for example in the quality control of assembly line products and in applications, where the traditional three-chromaticity colour measurements are not accurate enough. Spectral imaging produces large amounts of raw data which will be processed later in various applications. Image compression provides a possibility to reduce the amount of raw data for storing and transmission purposes. The image compression can be either lossless or lossy. In the lossy compression the quality of the reconstructed data should be estimated to evaluate the usefullness of the reconstructed data. The lossy compression is justified in the sense that the compression ratios are much higher than in the lossless case where the reconstructed data is identical to the raw data.

Spectral images are now available for different applications due to the development in the spectral imaging systems (Hauta-Kasari et al., 1999; Hyvärinen et al., 1998). Geoscience and remote sensing have been the main application areas of spectral images but nowadays several new application areas have emerged in industry. For example, applications in quality control, exact colour measurement, and colour reproduction use spectral information, since RGB colour information only is not sufficient.

Image compression has been one of the main research topics in image processing. The compression methods are usually developed for images visible to humans, i.e. for grey-scale or RGB colour images. Applications in the field of remote sensing and recent advances in industrial applications, however require the compression of spectral images (Vaughn & Wilkinson, 1995). Some compression methods are lossless (Memon et al., 1994; Roger & Cavenor, 1996), but most of the methods are lossy (Abousleman et al., 1997; Gelli & Poggi, 1999). Some applications can accept data which is compressed by a lossy scheme, but naturally the important features in the data must be present. If the lossy compression method cancels out any of the important features for the applications, then the lossless compression is the only possibility to decrease the amount of the raw data.

Compression is required due to the large amounts of data captured in the images. Regular digital cameras in everyday use apply JPEG or TIFF-compression. Images displayed in web-

Source: Vision Systems: Segmentation and Pattern Recognition, ISBN 987-3-902613-05-9,
Edited by: Goro Obinata and Ashish Dutta, pp.546, I-Tech, Vienna, Austria, June 2007

pages are compressed with the same methods. Compression in these applications is accepted as a normal procedure as long as the visual quality is not reduced.
With spectral images the memory or the transmission requirements are very high. Observations of Earth in spatial, spectral, temporal and radiometric methods produce data volume which is growing faster than the transmission bandwidth (Abousleman et al., 2002; Aiazzi et al., 2001). This means, that for long term storing or transmission, these databases should be compressed. The compression should be such that the spatial and spectral quality of the reconstructed image is high enough for the application. Table 1 shows examples of spectral imaging systems developed for remote sensing (Kerekes &Baum, 2002; Lillesand & Kiefer, 2000; AVIRIS, 2006; HyMap, 2006; HYDICE, 2006; Landsat, 2006; Hyperion 2006; Ikonos, 2006; OrbView, 2006; Aisa Eagle, 2006).

Name	# of channels	Spatial resolution, m	Radiometric resolution, bits	Raw data: kB/km^2
Airborne				
M7	12	10	8	120
AVIRIS	224	20	12	840
HYDICE	210	3	12	35000
HyMap	200	2	16	100000
Aisa Eagle	244	0.5	12	1400000
Spaceborne				
ERTS/MSS	4	80	8	0.6
Landsat/TM	7	30	8	7.8
Hyperion/EO-1	220	30	12	366.7
IKONOS	4/1	4/1	11	1719
OrbView-5	4/1	1.64/0.41	11	2045
OrbView-4	200	8	8	31250

Table 1. Examples of remote sensing systems. The spatial resolution for airborne sensors depends on the flight altitude. kB means kilobytes.

As an example, one spectral Airborne Visible/Infrared Imaging Spectrometer (AVIRIS) (AVIRIS, 2006) tape, taken in one day, can have up to 16 GB of raw data. Large amounts of data are also recorded in an application for the quality control of ceramic tiles (Kälviäinen et al., 1998): imaging of 25 ceramic tiles made up a spectral database of size 312 megabytes. Nowadays, there are several conferences where new spectral imaging systems for industrial applications are presented (MCS, 2006; EI, 2006; IGARSS, 2006).
When the client's application is known in advance the data for it can be extracted from the original database. For example, in mineral mapping the spectral range from around 2.0µm to 2.5µm is sufficient. Infrared systems utilize also a narrow band above the visual range for example in night time vision systems. If the colour features are enough, one can extract 30 bands out of 224 from the AVIRIS images for that specific application. In all previous cases and for various client requirements, the high quality database or even the original database must be present for the data extraction.

As the imaging systems have developed, at the same time the resources for storing the images are advanced due to the technological changes. In Table 2 we show some development features in hard drive technologies and properties (Thompson & Best, 2000; Hughes, 2002; Grochowski & Halem, 2003; Moreiro, 2006).

Feature	1970	1980	1990	2000	2009
Density, Mb/cm^2	$1*10^0$	$5*10^1$	$3*10^2$	$4*10^4$	$5*10^5$
Internal data rate, Mb/s	0.8	2	4	50	200
Capacity, GB	0.03	0.3	1	100	1600
Price, $/MB	NA	200	8	0.05	<0.002

Table 2. Advances in hard drive features. NA stands for information Not Available.

A similar growth pace as for the hard disk drives is experienced also in digital transmission both in wired and wireless cases: in average, every fifteen years the capacities have become thousand-fold.

The spectral imaging systems produce a vector of values for each pixel of the image. The values depend on the resolution of the imaging system and they are normally presented as 8 bit, 12 bit or 16 bit values. Thus, a spectral image can be considered as a set of two-dimensional, equal size images. Now, compression methods can be similar to the methods applied to greyscale images or to RGB-colour images. For lossless compression also regular text compression methods can be applied. This simple approach may be usable, when a) the original image should be perfectly reconstructed, b) the compression method should be widely available, and c) high compression ratios are not required. These methods include entropy modelling followed by Huffman coding, arithmetic coding or Burrows-Wheeler transform. The standard Unix tool, gzip, is based on Lempel-Ziv coding (Ziv & Lempel, 1977). It gives the average lossless compression ratio 1.41 for a set of four Moffet Field scenes and 1.39 for a set of five Jasper Ridge scenes from the AVIRIS dataset (AVIRIS, 2006). Much better lossless compression ratios are received if the composition of the spectral images is observed. Best lossless compression methods are most often based on predictive coding combined with entropy modeling (Aiazzi et al., 2002; Aiazzi et al., 2001; Aiazzi et al., 1999; Benazza-Benyahia et al., 2001; Mielikäinen & Toivanen, 2003; Mielikäinen, 2006). Also integer transforms (Kaarna, 2001) or lossless vector quantization (Ryan & Arnold, 1997-1) is possible for the perfect reconstruction.

A lossy compression procedure for spectral images consists of three phases. The first phase decorrelates the raw data in spatial and spectral dimensions, the second phase quantizes the coefficients from the first phase. The third phase utilizes some lossless scheme to encode the quantized coefficients. This procedure is depicted in Fig. 1.

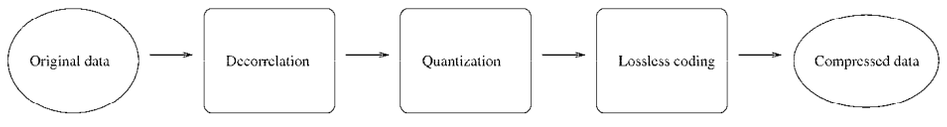

Fig. 1. The three phases in the lossy compression.

A compression procedure is of any practical interest only if it has an inverse procedure which reconstructs the original data or image. An inverse procedure includes the same phases as the compression procedure in Fig. 1, but they are processed in reverse order. First, the compressed data is decoded resulting in the quantized coefficients. Then the quantized coefficients are restored to their original values and these values compose the original data. In Fig. 2 the decompression, the inverse procedure for compression, is depicted.

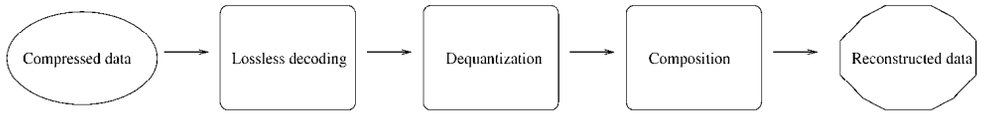

Fig. 2. Decompression, the inverse procedure for compression.

Different methods and their parameter values are possible in the compression procedure. Depending on the selections the reconstructed data can be equal to the original data or some information can be lost. The methods and parameters are selected such that the important features of the image are present and the information lost can be regarded as an observation noise or otherwise irrelevant for the application. The evaluation of the quality of the reconstructed data is necessary when using lossy compression. The quality measurements are most often based on the pixelwise or bandwise difference between the original image and the reconstructed image resulting to logarithmic signal-to-noise ratio (Rabbani & Jones, 1991). Specific measures for spectral images include both the percentage maximum absolute distortion measure (PMAD) (Ryan & Arnold, 1997-2; Ryan & Arnold, 1998) and the blockwise distortion measure for multispectral images BDMM (Kaarna & Parkkinen, 2002). PMAD guarantees that every value in the reconstructed image is within a maximum distance from the original value. The maximum distance is relative to the original value. BDMM correlates blockwise filtering of the original and the reconstructed image to the visual quality of the distorted images.

In the following sections we introduce methods for lossy and lossless compression of spectral images. Then we describe how to evaluate the quality of reconstructed data in the lossy case. Finally, we show experimental results and evaluate different compression methods.

2. Lossy compression of spectral images

A comprehensive study on theoretic aspects of lossy source coding can be found from (Berger & Gibson, 1998). Data compression is thoroughly considered in (Donoho et al., 1998). Both scalar and vector quantization is widely surveyed in (Gray & Neuhoff, 1998). The wavelet transform is described in detail in (Daubechies, 1992; Taubman & Marcellin, 2002).

Lossy compression methods achieve remarkably higher compression ratios than lossless compression by neglecting some unessential data in the compression phase. Several lossy compression methods have been developed for the compression of spectral images. Some of them are two-dimensional methods applied separately to each band of the spectral image

(Abousleman et al., 1994), and some methods have been further enhanced from the two-dimensional methods to be three-dimensional (Abousleman et al., 1997; Kaarna & Parkkinen 1999). Most of the recent methods apply separate subtasks to the spectral and spatial dimensions due to their dissimilar characteristics (JPEG2000, 2006; Aware, 2006; Kaarna et al., 2000; Kaarna et al., 2006).
A rough classification of the compression methods for the spectral images include the principal component analysis (PCA) for the decorrelation of the spectral data, the wavelet transform for the spatial compression of images, predictive methods applied simultaneously to the spectral and spatial dimensions of the image, and finally the vector quantization of the spectra in the image. Each of these methods can alone compress the image, but in practise, best compression results are obtained through combining these methods.

2.1 Vector quantization

Clustering is an unsupervised method to classify patterns in an image. Patterns within a cluster are more similar to eachother than they are to a pattern belonging to another cluster. Thus, a lossy compression method can be established on that notation: each member of a cluster are represented by the cluster center. The compressed data consists of cluster centers and an index image.
Vector quantization utilizies the previous idea (Ryan & Arnold, 1997-1; Ryan & Arnold, 1997-2). First, a decomposition of the image into a set of vectors is performed. With spectral images the decomposition naturally consists of the spectral vectors. Then a codebook is generated from a training set of vectors using an iterative algorithm. Finally, each spectral vector of the image is quantized to the closest vector in the codebook according to the selected distortion measure. The compressed data consists of a codebook and a set of indices to the codebook. One index is required for each spectrum of the image.
The generalized Lloyd algorithm (GLA) tries to optimize the codebook *C*. The algoritmic presentation of the GLA is :

Algorithm 1:

Step 1: Select the initial codebook C_1, set $m=1$.
Step 2: With the given codebook C_m perform one iteration to generate an improved codebook C_{m+1}.
Step 3: Compute the average distortions for C_{m+1}. If the change from the previous iteration is small enough, then stop.
Otherwise set $m = m+1$ and continue from Step 2.

The Step 2 of Algorithm 1 is generally implemented using a Nearest Neighbor condition:
Algorithm 2:
Step 1: Using the codebook $C_m = y_i$ partition the training set T into clusters R_i with the NN condition: $R_i = \{ x \in T : d(x,y_i) \leq d(x,y_j);\ all\ j \neq i \}$.
Step 2: Compute the centroids for the clusters $\{cent(R_i)\}$ to obtain an improved codebook $C_{m+1} = \{cent(R_i)\}$.

In vector quantization each vector is represented by the centroid of a cluster it belongs to. The resulted data from the VQ consists of the cluster centroids and of an index image, which

describes the inclusion of each vector into one cluster. In Fig. 3. we illustrate the vector quantization for the compression of spectral images.

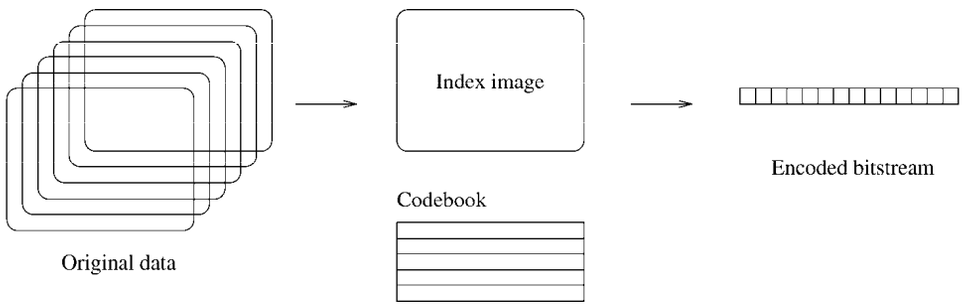

Fig. 3. Vector quantization in lossy compression of spectral images.

Similar approach to vector quantization was defined in (Toivanen et al., 1999). The procedure produced an index image and a codebook which was generated with a Self-Organizing Map (SOM). The results were good compared to a clustering method in (Kaarna et al., 1998).

Even though vector quantization is theoretically optimal in lossy coding, the implementation issues constrain the performance (Poggi & Ragozini, 2002). Computational complexity and memory requirements have been the main drawbacks that have been attacked (Poggi & Ragozini, 2002; Kaarna et al., 2000; Ryan & Arnold, 1997-2; Kamano et al., 2001).

A tree-structured product-codebook was designed to support progressive transmission (Poggi & Ragozini, 2002). In product-codebook VQ, all codewords are of type $x_{ij} = u_i * v_j$, where * is the decomposition rule. The component codebooks were organized in a tree-structure in order to speed up the codeword selection. The optimal design of the components codebooks is a complex task, but a suboptimal solution clearly lowered the computational requirements. A tree-structure was also applied in (Kaarna et al., 2000) to accelarate the look-up functions in clustering. The leaves of the tree consisted of short linear lists and the search operation combined both the tree-structured and linear look-up functions.

An important feature in vector quantization is how to define an appropriate distortion measure for two vectors (Ryan & Arnold, 1997-2). The Euclidian distance between the two vectors X and Y is defined as

$$E = \sqrt{\sum_{i=1}^{N} (x_i - y_i)^2} \tag{1}$$

where x_i and y_i are components of vectors X and Y, respectively. A drawback for the Euclidian distance is that it doesn't account for the various shapes of the vectors. The PMAD distortion measure was developed to guarantee that every pixel $B'(s_1,s_2,\lambda)$ of the compressed and reconstructed image is within a maximum distance of $p*100\%$ from its original value $B(s_1,s_2,\lambda)$, i.e. $(1-p)B(s_1,s_2,\lambda) < B'(s_1,s_2,\lambda) < (1+p)B(s_1,s_2,\lambda)$. Using this distortion measure, lossy compression ratios cr up to $cr=17$ were received with airborne multispectral images.

One large codebook can be replaced with two codebooks (Kamano et al., 2001). The first one, a relative small codebook, with few training sets was generated. The second codebook was generated from the residual data between the original image and the first codebook output. The proposed scheme improved the coding efficiency and reduced the transmission rate according to the numerical experiments.

2.2 Spectral decorrelation with PCA

In image compression, the principal component analysis (PCA) produces optimal results in the sense of the mean-square error reconstruction (Karhunen & Joutsensalo, 1995).
The principal component analysis is based on the covariance matrix $C = E[(x-\mu)(x-\mu)^T]$, $\mu = E[x]$ of the original data. In practical calculations the matrix C is replaced by an estimated $\hat{C}$

$$\hat{C} = \frac{1}{n}\sum_{i=1}^{n}(x_i - \mu^*)(x_i - \mu^*)^T \tag{2}$$

where x_i is a sample vector and μ^* is the estimated mean vector of the sample set. The sum is over all the n samples of the set. From the estimated $\hat{C}$ the eigenvalues $\lambda_1, \lambda_2, ..., \lambda_n$ and the respective eigenvectors $u_1, u_2, ..., u_n$ are calculated. Due to the properties of the autocorrelation matrix, the eigenvalues λ_i , $i=1,n$ are all real and nonnegative.
As soon as the eigenvalues λ_i are known and without loss of generality the indexing is such that $\lambda_1 > \lambda_2 > ... > \lambda_n$, the reconstruction x^* of x is obtained as

$$x^* = \sum_{i=1}^{p}(x^T u_i)u_i \tag{3}$$

where p, $p < n$ is selected such that the required quality in reconstruction will be achieved. In Fig. 4 the principle of the PCA compression of spectral images is shown.

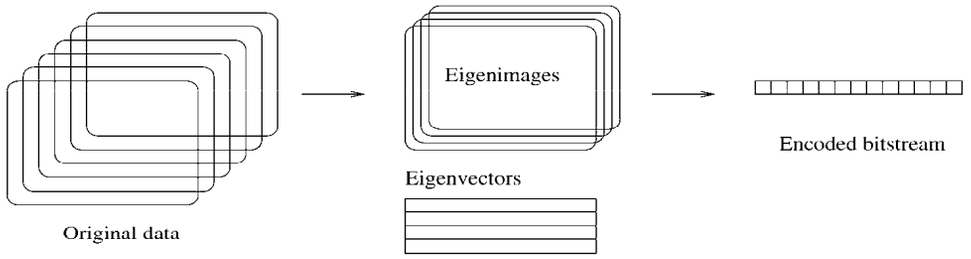

Fig. 4. The PCA in lossy compression of spectral images. In this example, the number p of eigenimages/eigenvectors is $p=4$.

2.3 Transform coding

Function transforms have been used for centuries to solve problems i.e. in mathematics, physics and engineering (Zayed, 1996). For example, in audio signal processing it would be interesting to know what frequencies are included in the measured signal. This problem can be solved using the Fourier transform.

In general, a transform is a mathematical operation where a function or data *f* in domain *u* is transformed into another function or data *F* in domain *U*: $f \rightarrow F$. The purpose of the transform is normally one of the following:

- After the transform it would be easier to solve the original problem.
- The transformed data gives a new insight to the problem at hand.
- The data in the domain *F(U)* is measured experimentally and the function *f* needs to be constructed from this data.

The transforms $f \rightarrow F$ of any practical value has an inverse transform, where the original function *f* is completely constructed from *F*, i.e. $F \rightarrow f$. Thus, the transform pair is used to solve the original problem using data *F* in domain *U*, and then the solution is transformed back to the data *f* in domain *u*.

A popular transform in engineering is the Fourier transform. The transform was developed by Joseph Fourier in 1822 as he demonstrated, that most signals of practical interest can be expanded into a series of sinusoidal functions. Later on, this continuos transform has been developed to be applicable in discrete computations (Proakis & Manolakis, 1994).

The wavelet transform f^w of a function *f(t)* also provides a time-frequency localization (Chui, 1992; Daubechies, 1988; Daubechies, 1992; Mallat, 1998; Vetterli & Kovačević, 1995) as

$$f^w(a,b) = |a|^{-1/2} \int f(t)\psi\left(\frac{t-b}{a}\right)dt \tag{4}$$

where ψ is called a mother wavelet with zero average, $\int\psi(t)dt = 0$. The mother wavelet ψ(t) is defined as a double-indexed function as

$$\psi^{a,b}(t) = |a|^{-1/2}\psi\left(\frac{t-b}{a}\right) \tag{5}$$

Practical applications, like the signal compression, require fast implementations. In signal processing community, the wavelet transform is implemented with convolution as an filtering operation and the conjugate mirror filters are used as filter banks. The orthogonal wavelet transform is implemented by the cascading conjugate mirror filters. The perfect reconstruction is achieved with this implementation. The orthonormal bases of wavelets can be constructed using multiresolution analysis.

The fast discrete wavelet transform is computed using perfect reconstruction filter banks. Vetterli showed (Vetterli, 1986), that perfect reconstruction was always possible using FIR-filters. The multiresolution approximation lead to two discrete, finite length filters, and, thus, a filter bank was a solution to a fast implementation.

Using the definition

$$f(t) = \sum_{n=-\infty}^{\infty} a_0[n]\phi(t-n) \in V_0 \tag{6}$$

where $\phi(t)$ a is the scaling function, and due to the properties of multiresolution, $\{\phi(t-n)\}_{n \in Z}$ is orthonormal, then

$$a_0[n] = \langle f(t), \phi(t-n) \rangle \tag{7}$$

The approximation a_{j+1} in the next coarser level of the multiresolution is obtained by

$$a_{j+1}[p] = \sum_{n=-\infty}^{\infty} h[n-2p]a_j[n] \tag{8}$$

and the difference d_{j+1} between the two levels by

$$d_{j+1}[p] = \sum_{n=-\infty}^{\infty} g[n-2p]a_j[n] \tag{9}$$

where $g[n]$ is defined using the discrete filter $h[n]$ as

$$g[n] = (-1)^{1-n} h[1-n] \tag{10}$$

At the reconstruction of the data the coefficients are obtained as

$$a_j[p] = \sum_{n=-\infty}^{\infty} h[p-2n]a_{j+1}[n] + \sum_{n=-\infty}^{\infty} g[p-2n]d_{j+1}[n] \tag{11}$$

and finally, the discrete values f_d of the original function are recovered from

$$f_d[p] = \sum_{n=-\infty}^{\infty} a_0[n]\phi_d[p-n][n] \tag{12}$$

Since the scaling and the wavelet filters h ang g are finite, the infinite sums in Eqs. 8-12 are computed using the convolution. The discrete wavelet transform is illustrated in Fig. 5: part a) shows the transform and part b) the inverse transform.

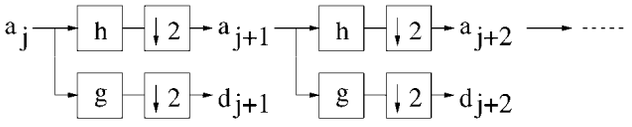

a)

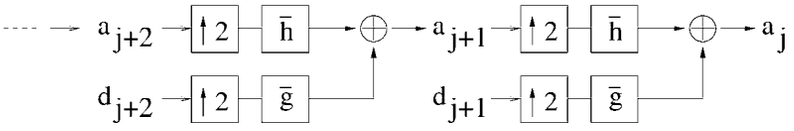

b)

Fig. 5. The discrete wavelet transform: a) the transform, b) the inverse transform.

The transform coefficients are the values of a_{j+N} and d_{j+i}, $i=1,...,N$. Downsampling by two (↓2) is performed in the transform and upsampling by two (↑2) in the inverse transform. In practice, Eq. 12 is not used and the values for a_0 are obtained directly as discretized values $f[n]$ of $f(t)$. Due to the perfect reconstruction property, the inverse transform returns the discretized values $f[n]$ directly as coefficients a_0.

The orthogonal, compactly supported wavelets described above has several enhancements. They include biorthogonal wavelets (Cohen et al., 1992), which allow symmetric wavelets.

This was a result of a modification in the multiresolution approximation. Another modification in the multiresolution lead to the wavelet packet analysis (Coifman & Wickerhauser, 1992). Wavelet packets are described as a full transform of the coefficients. Since in the original transform only the coefficients a_j are transformed, see Fig. 5, then in the wavelet packet analysis also the coefficients d_j are transformed in a similar way.

2.4 Linear and non-linear compression

The principal component analysis (PCA) is a widely used statistical technique in pattern recognition, image processing, and signal processing. PCA is an optimal solution in minimization of the mean-square representation error $E\{||x - x^*||^2\}$ where the data x is approximated using a lower dimensional linear subspace x^* (Karhunen & Joutsensalo, 1995). The principal component analysis provides orthonormal basis functions that optimally decorrelate the data. Other methods, like DCT or wavelets, approximate this optimal decorrelation. The justification for the wavelet transform in signal compression comes from the nonlinear approximation (Daubechies, 1998; Donoho et al., 1998; Devore et al., 1992), where the linear combination of N basis functions is used instead of the first N basis functions. In the linear approximation, the space S_n spanned by the first N basis functions Φ_n is

$$S_n = \left\{ \sum_{n=1}^{N} c_n \Phi_n ; c_n \in C \right\} \tag{13}$$

and in the nonlinear approximation the space S_n is

$$S_n = \left\{ \sum_{n} c_n \Phi_n ; c_n \in C, \#\{n, c_n \neq 0\} \leq N \right\} \tag{14}$$

In nonlinear approximation the wavelet coefficients are ordered according to their significance and the most significant coefficients and their addressing are included in the bit stream.

2.5 Nonlinear compression through the three-dimensional wavelet transform

In two-dimensional case the construction of the wavelet transform starts from a tensor product of two one-dimensional multiresolution analyses (Daubechies, 1992; Mallat, 1989), $\boldsymbol{V_0} = V_0 \otimes V_0$, where V_j, $j \in Z$ is a multiresolution of $L^2(R)$. The multiresolution ladder is similar to that of one-dimensional case,, and now the multiresolution is

$$\begin{aligned} &(1) \quad \ldots V_2 \subset V_1 \subset V_0 \subset V_{-1} \subset V_{-2} \ldots \\ &(2) \quad V_0 = V_0 \otimes V_0 \\ &(3) \quad F \in V_j \Leftrightarrow F\left(2^j \cdot, 2^j \cdot\right) \in V_0, F(x_1, x_2) = f(x_1) f(x_2), f, g \in V_0 \end{aligned} \tag{15}$$

and the product

$$\Phi_{0,n,m}(x_1, x_2) = \phi_{0,n}(x_1) \phi_{o,m}(x_2) = \phi(x_1 - n) \phi_{0,m}(x_2 - m), n, m \in Z \tag{16}$$

is an orthonormal basis for $\boldsymbol{V_0}$. The basis for $\boldsymbol{V_j}$ is obtained (Mallat, 1998) as

$$\Phi_{j,n,m}(x_1,x_2)=\phi_{j,n}(x_1)\phi_{j,m}(x_2)=\frac{1}{2^j}\Phi(2^{-j}x_1-n)\Phi(2^{-j}x_2-m) \tag{17}$$

The orthogonal complement in V_{j-1} for V_j is W_j

$$\begin{aligned} V_{j-1}&=V_{j-1}\otimes V_{j-1}=(V_j\oplus W_j)\otimes V_j\oplus W_j\\ &=V_j\otimes V_j\oplus\left[(V_j\otimes W_j)\oplus(W_j\otimes V_j)\oplus(W_j\otimes W_j)\right]\\ &=V_j\oplus W_j \end{aligned} \tag{18}$$

and, thus, W_j consists of three parts, whose bases Ψ are combinations of one-dimensional scaling function ϕ and wavelet function ψ:

$$\begin{aligned} \Psi^h(x_1,x_2)&=\phi(x_1)\psi(x_2)\\ \Psi^v(x_1,x_2)&=\psi(x_1)\phi(x_2)\\ \Psi^d(x_1,x_2)&=\psi(x_1)\psi(x_2) \end{aligned} \tag{19}$$

The set $\{\Psi^{\lambda}_{j,n};\ j\in Z,\ n\in Z^2,\ \lambda=h,v,d\}$ is an orthonormal basis for $L^2(R^2)$ (Daubechies, 1992). In this construction the sampling is done separately in vertical and horizontal directions, but the wavelet bases are nonseparable.

The fast two-dimensional wavelet transform is performed using filtering operations on vertical and horizontal dimensions of the image. The original image is filtered into quadrants and then the approximation quadrant is filtered further on. If the size of the original image in $N * N$ then each quadrant is of size $N/2 * N/2$. The transform has the perfect reconstruction property.

Similar approach as in the two-dimensional case gives the three-dimensional wavelets that are applied to the three-dimensional data like spectral images. If the separation of the spectral dimension is not applied, then the multiresolution analysis gives the configuration for the transform as

$$\begin{aligned} V_{j-1}&=V_{j-1}\otimes V_{j-1}\otimes V_{j-1}\\ &=(V_j\oplus W_j)\otimes(V_j\oplus W_j)\otimes(V_j\oplus W_j)\\ &=(V_j\oplus W_j)\otimes\{(V_j\otimes V_j)\oplus(V_j\otimes W_j)\oplus(W_j\otimes V_j)\oplus(W_j\otimes W_j)\}\\ &=(V_j\otimes V_j\otimes V_j)\oplus\\ &\quad\{(V_j\otimes V_j\otimes W_j)\oplus(V_j\otimes W_j\otimes V_j)\oplus(V_j\otimes W_j\otimes W_j)\oplus\\ &\quad(W_j\otimes V_j\otimes V_j)\oplus(W_j\otimes V_j\otimes W_j)\oplus(W_j\otimes W_j\otimes V_j)\oplus(W_j\otimes W_j\otimes W_j)\} \end{aligned} \tag{20}$$

The scaling function for the basis V_0 is

$$\Phi_{0,n_1,n_2,n_3}(x_1,x_2,x_3)=\phi(x_1-n_1)\phi(x_2-n_2)\phi(x_3-n_3),\quad n_1,n_2,n_3\in Z \tag{21}$$

and the filtering of the spectral image is done using one scaling function and seven wavelets, which are defined as

$$
\begin{aligned}
\Phi^{s,a}(x_1,x_2,x_3) &= \phi(x_1)\phi(x_2)\phi(x_3)\\
\Psi^{h,a}(x_1,x_2,x_3) &= \phi(x_1)\phi(x_2)\psi(x_3)\\
\Psi^{v,a}(x_1,x_2,x_3) &= \phi(x_1)\psi(x_2)\phi(x_3)\\
\Psi^{d,a}(x_1,x_2,x_3) &= \phi(x_1)\psi(x_2)\psi(x_3)\\
\Psi^{s,d}(x_1,x_2,x_3) &= \psi(x_1)\phi(x_2)\phi(x_3)\\
\Psi^{h,d}(x_1,x_2,x_3) &= \psi(x_1)\phi(x_2)\psi(x_3)\\
\Psi^{v,d}(x_1,x_2,x_3) &= \psi(x_1)\psi(x_2)\phi(x_3)\\
\Psi^{d,d}(x_1,x_2,x_3) &= \psi(x_1)\psi(x_2)\psi(x_3)
\end{aligned}
\tag{22}
$$

where all dimensions are dilated similarly and the sampling is done separately along each dimension of the three-dimensional image. The original spectral image of size $N * N * N$ is filtered into octants of size N/2 * N/2 * N/2 as illustrated in Fig. 6.

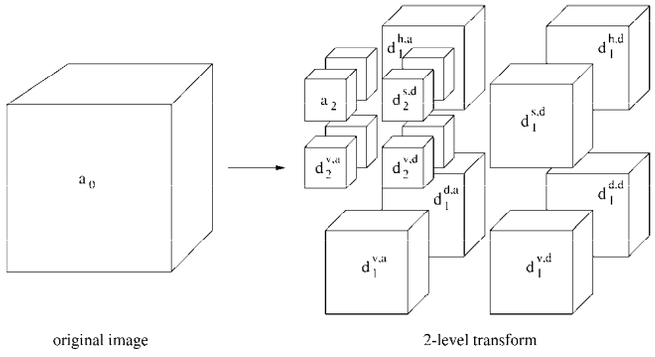

a)

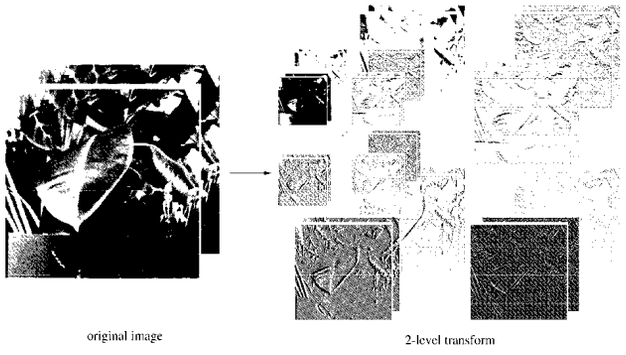

b)

Fig. 6. Three-dimensional wavelet transform applied twice. a) The principle of the transform, the coefficients *a* come from the low-pass filtering and the coefficients *d* from the high-pass filtering. b) Three-dimensional transform applied to one Bristol-image (Parraga et al., 1998).

Similar procedure will produce wavelets in higher dimensions than three. A theorem says (Mallat, 1998) that the family obtained by dilating and translating the 2^p-1 wavelets for $\alpha \neq 0$

$$\left\{ 2^{-\frac{pj}{2}} \Psi^{\alpha}\left(\frac{x_1 - 2^j n_1}{2^j}, \ldots, \frac{x_p - 2^j n_p}{2^j} \right) \right\}_{1 \le \alpha < 2^p, (j, n_1, \ldots, n_p) \in Z^{p+1}} \tag{23}$$

is an orthonormal basis for $L^2(R^p)$. The configuration of the three-dimensional transform in Eqs. 20, 21, and 22 is compatible with this theorem.

The multiwavelet based transform is slightly more complicated due to preprocessing, computations, and housekeeping (Kaarna & Parkkinen, 1999). This transform has similar variants as the scalar case above. The multiwavelet transform with two scaling functions compatible with Eq. 22, Fig. 6 would contain the coefficients of the first scaling function in the front part of each cubic block and the coefficients from the second scaling function in the back part of each cubic block. The similar division applies to the coefficients from the two wavelet functions.

2.6 Linear compression through spectral decorrelation and spatial compression

A reference method for image compression is based on the principal component analysis (PCA) as a spectral decorrelation method combined with a two-dimensional transform as the spatial compression method. Both the discrete cosine transform (Rabbani & Jones, 1991) and the wavelet transform are used as the spatial compression methods (Kaarna & Parkkinen, 2001). Also the discrete cosine transform has been enhanced to the hyperspectral images (Abousleman et al., 1995).

In Fig. 7 we illustrate the compression method, where the spectral decorrelation by PCA is followed the spatial wavelet transform.

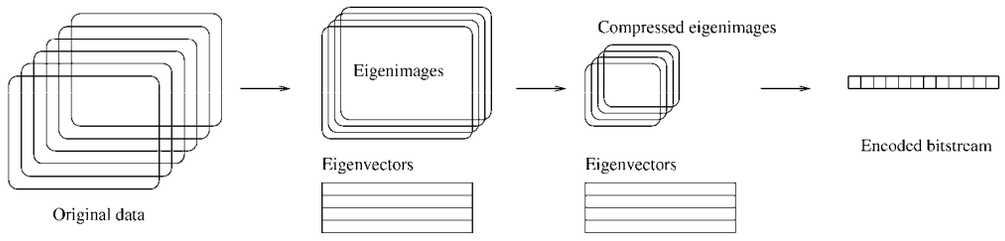

Fig. 7. PCA and the 2D wavelet transform in the lossy compression of spectral images.

The new image compression standard, JPEG2000 was basically defined only for colour images, but the Part 2, extensions, includes also transforms for multiple component imagery (Taubman & Marcellin, 2002). The linear block transform can be considered as a matrix multiplication as described in Section 2.2 as the PCA transform. The multiplication has an inverse operation and, thus, the data can be reconstructed. Also the wavelet transform is defined suitable for a point transform in JPEG2000. The work is currently underway, so the exact definitions are open (Taubman & Marcellin, 2002; JPEG2000, 2006).

2.7 Encoding in the Lossy Compression

The encoding phase of the compression is accomplished in a lossless manner, see Fig. 1. In encoding the quantized coefficients are coded to minimize the amount of data to be stored or transmitted. In addition, the new representation should contain the same information as the original data. In decoding the new representation is coded back to the original data. The encoding methods are divided into statistical methods and dictionary methods. In statistical methods, like static Huffman coding and arithmetic coding, the probabilities of the source symbols are required and two passes of the source are needed for encoding. In dictionary based methods, adaptive methods like the Ziv-Lempel-algorithms LZ77 and LZ78, only one pass is sufficient for encoding (Lelewer & Hirschberg, 1987; Ziv & Lempel, 1977; Ziv & Lempel, 1978).

In LZ77 (Ziv & Lempel, 1977), the source characters were encoded using a window of length *N*. The first *N-F* source symbols were already encoded and the last *F* source symbols constituted a lookahead buffer. The next source symbols in the lookahead buffer *F* were encoded by searching the longest match from the *N-F* source symbols in the window *N*. The match was coded using a pointer and the length of the match. In decoding, no search was needed, since the data was copied from the pointer position (Lelewer & Hirschberg, 1987; Ziv & Lempel, 1977). A modification to the previous method is the LZ78-encoding (Ziv & Lempel, 1978; Bell et al., 1989). Now the source symbols seen so far are split into phrases, where each phrase is the longest matching phrase seen so far plus one source symbol. Each phrase is coded as an index to its prefix plus the extra symbol. The new phrase is also added to the list of phrases that may be referenced. After the introduction of the original LZ-methods, there have appeared several enhancements and modifications to these methods, see e.g. (Bell et al., 1989; Lelewer & Hirschberg, 1987).

In arithmetic coding the source symbols are coded to a magnitude in range *[0,1)* (Langdon, 1984; Rissanen & Langdon, 1979). Initially, the range was split by the probabilities of single source symbols. New source symbols split the existing subranges in a similar way. Finally, all source symbols were manipulated and the subranges gave the codes. The encoding carried the prefix property. In decoding, the model of the source used by the encoder must be known. The encoded value was compared to the known probabilities in range *[0, 1)*, then in the subranges, and finally the decoder output the original source symbols.

SPIHT (Said & Pearlman, 1995) is an effective wavelet-based compression method for two-dimensional images. Color images are compressed through applying the method in each R, G, and B-band separately. For spectral images this approach has been extended to simultaneously manipulate all the bands of the spectral image (Dragotti et al., 2000). The approach combines the wavelet transform with the coding of the selected wavelet coefficients. The wavelet coefficients are coded using a hierarchical tree structure. In Fig. 8, the two-dimensional tree structure is depicted. In the three-dimensional case the structure is extended to include also the spectral dimension. Then the two-dimensional "squares" of coefficients become three-dimensional "cubics". The extension is analogious to that depicted in Fig. 6 for the wavelet transform.

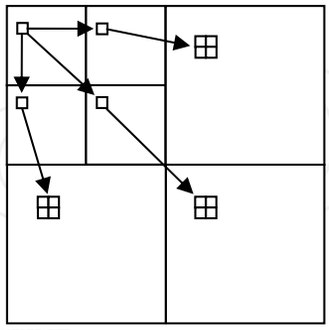

Fig. 8. The tree structure in 2D SPIHT.

2.8 Results from lossy compression

In the experiments we applied the integer PCA and wavelet transform to four AVIRIS images: Jasper Ridge, Moffet Field, Lunar Lake, and Cuprite (AVIRIS, 2006). The spatial size of each image was 608*512 and the number of bands was 224. The resolution of the original images was 16 bits. Thus, each image occupied 139,460,608 bytes of disk space in the raw form. Band 200 from Moffet Field image is displayed in Fig. 9.

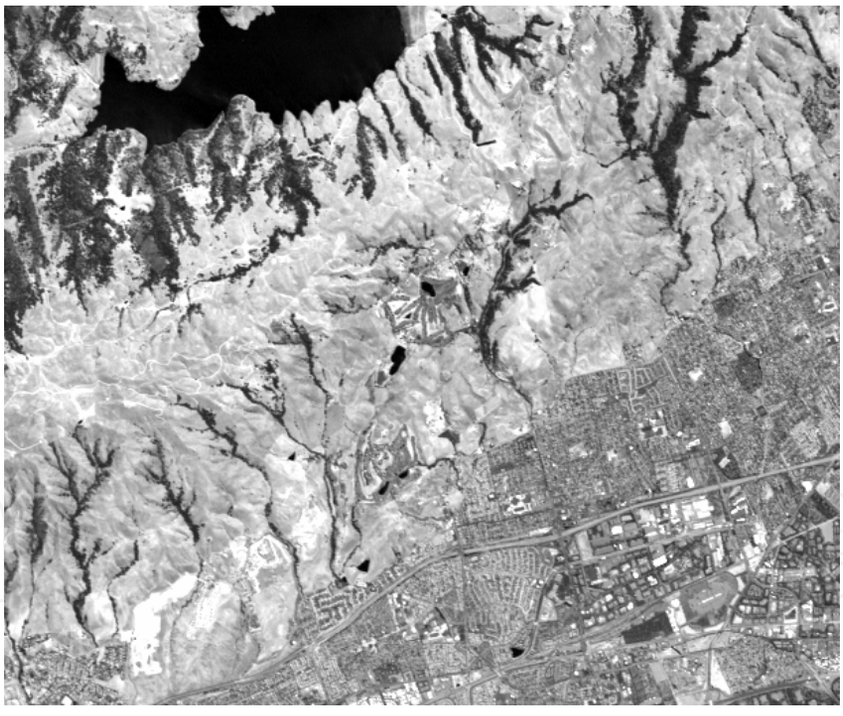

Fig. 9. Spectral band 200 from Moffet Field AVIRIS image.

In Fig. 10 the results from the PCA decorrelation with the 2D wavelet tranform are shown, see Fig 7. With PCA, the variable-bit-rate approach was also applied: the bit-allocation

between the eigenimages was entropy-based (Kaarna et al., 2006). The results from the 3D wavelet transform are also included, see Fig. 6. The horizontal axis is the compression ratio (CR) and the reconstruction quality as PSNR in *dB* (Eq. 28) is in the vertical axis.

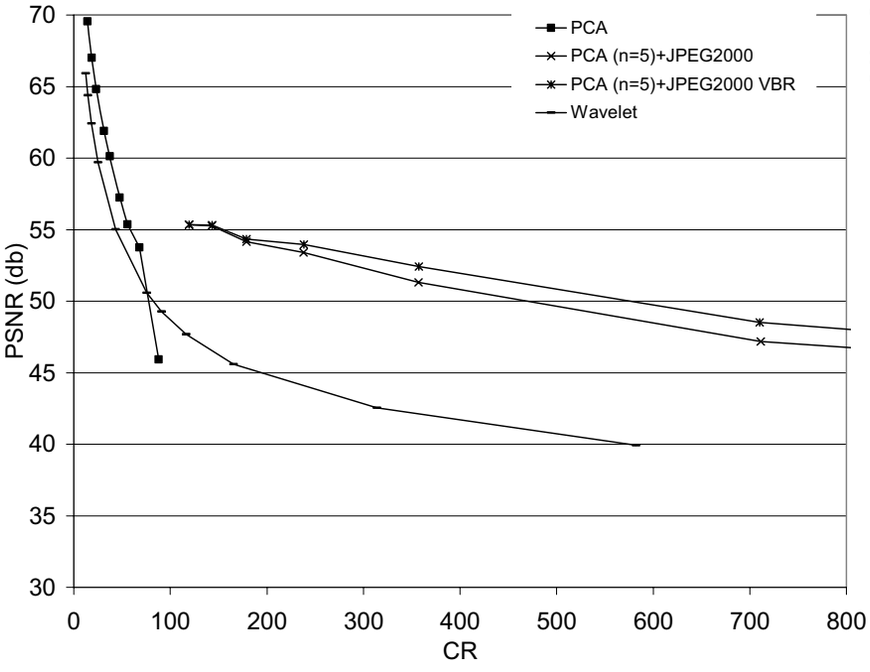

Fig. 10. Results from the lossy compression of AVIRIS spectral images. In PCA, $p=5$ (Eq. 3).

3. Lossless compression of spectral images

The lossless compression is also called image coding when all the information in the image is included in the bit stream and the representation of the information is changed into a more compact form. In lossless compression of the spectral images the methods described in Section 2.7 can be used, since they are universal coding approaches for any digital information. These entropy-based textual coding approaches produced compression ratios from 1.5 to 2.0 for a set of AVIRIS-images (Kaarna & Parkkinen, 2001).

For spectral images, the lossless compression can be done by vector quantization and arithmetic coding (Ryan & Arnold, 1997-1). First, the vector quantization is applied to the spectra of the image; second, the residual image is created and then it is coded using arithmetic coding. The residual image contains only integer values obtained after rounding the difference between the closest vector center and the original spectral values. In addition, addresses from vector quantization and a set of other parameters are stored as side information. Also other lossless coding methods exist, e.g. they are based on band ordering (Tate, 1997; Toivanen et al., 2005) or spectral and spatial noncausal prediction (Memon et al., 1994). Thus, in the lossless compression of spectral images better results are achieved through the transform coding and especially, with the predictive coding.

3.1 Transform coding in lossless compression of spectral images

We applied the principal component analysis (PCA) to define the approximation image (Kaarna, 2001). PCA will produce a set of base vectors, which minimize the approximation error in the L^2-sense. The problem of heavy computations in PCA is solved by selecting only a small number of spectra from the image for the calculation of the base vectors. Also an integer version of PCA is needed. The calculation of the eigenvalues and eigenvectors is done with floating values, but the double precision results from the analysis are transformed to integer values such, that the required number of correct digits is maintained in the reverse transform. The PCA transform was described in Section 2.2.

Since the approximation image is available, then the residual image can be calculated. The residual image is then further compressed with the integer wavelet transform. Reversible integer-to-integer wavelet transforms have shown good performance in lossless colour and grey-scale image coding (Adams & Kossentini, 2000). The integer wavelet transform is based on the lifting scheme: different filters were derived by combining the prediction step with the update step (Calderbank et al., 1998). The integer wavelet transform is one-dimensional in nature. In the two-dimensional case, the one-dimensional transform is applied to the rows and columns of the image. In the three-dimensional case, the one-dimensional transform is applied to the spatial and spectral domains separately. The approach is the same as in the general case, see Fig. 8.

Similarly to the floating case, there exists different integer wavelet transforms (Adams & Kossentini, 2000; Calderbank et al., 1998; Daubechies, 1998). The oldest form of the integer wavelet transform subtracts the even samples from the odd samples to get the difference d_1 and the new approximation a_1 as

$$\begin{aligned} d_{1,l} &= a_{0,2l+1} - a_{0,2l} \\ a_{i,l} &= a_{0,2l} + \lfloor d_{1,l} / 2 \rfloor \end{aligned} \tag{24}$$

where the original data is stored in a_0. The second subscript refers to the index of the sample vector. The exact reconstruction comes from calculating the values in reverse order as

$$\begin{aligned} a_{0,2l} &= a_{1,l} - \lfloor d_{1,l} / 2 \rfloor \\ a_{0,2l+1} &= a_{0,2l} + d_{1,l} \end{aligned} \tag{25}$$

In general, the integer wavelet transform consists of the prediction and of the update based on the lifting where the number of vanishing moments is increased. In (Adams & Kossentini, 2000), the best lossless compression results for grey-scale images were obtained with the 5/3-transform, the forward 5/3-transform is defined as

$$\begin{aligned} d_{1,l} &= a_{0,2l+1} - \lfloor 1/2\left(a_{0,2l+2} + a_{0,2l}\right) \rfloor \\ a_{i,l} &= a_{0,2l} + \lfloor 1/4\left(d_{1,l} + d_{1,l-1} + 1/2\right) \rfloor \end{aligned} \tag{26}$$

where a_0 refers to the even samples and d_0 to the odd samples of the original signal. We implemented also other integer wavelet transforms, but the final results were calculated with the 5/3-transform.

The zero order entropies of the AVIRIS test images, see section 2.8, are tabulated in Table 3, column ent_o. The test images were compressed with the lossless Burrows-Wheeler algorithm (Nelson, 1996) and the bitrates are in Table 3, the second column (Bit-rate). The compression

results with the integer PCA and wavelet approach are shown also in Table 3 (Kaarna, 2001). The compression ratio (CR) is a ratio between the size of the original file size and the size of file containing the encoded image. The bitrate is calculated as 16 bits/sample divided by the compression ratio (column Bit-rate). The zero order entropy of the residual image is tabulated before (ent_b) and after (ent_a) the integer wavelet transform. Also, the entropy of all encoded data is tabulated (ent_f). All entropies are expressed as bits/sample. The last column (ratio) contains the compression ratio as the ratio between the original entropy and the entropy of all encoded data (ent_f).

Image	ent_o	Bit-rate	ent_b	ent_a	ent_f	CR	Bit-rate	ratio
Jasper	11.19	7.94	6.14	5.24	5.62	2.83	5.65	1.99
Moffet	11.55	8.11	6.38	5.36	5.74	2.79	5.73	2.01
Lunar Lake	12.17	7.07	5.84	5.14	5.50	2.79	5.73	2.21
Cuprite	12.07	7.29	6.12	5.15	5.51	2.90	5.52	2.19

Table 3. Entropies and actual compression ratios for the four test images.

Our test images were from the AVIRIS free data set. They were measured in 1997 and most of the comparative results were calculated using older AVIRIS data sets. Thus, the comparisons will give only suggestions on the coding properties of our method. The results from (Ryan & Arnold, 1997-1) are collected in Table 4.

Image	Original entropy	Final entropy	ratio
Jasper	9.79	5.73	1.71
Moffet	9.64	5.63	1.71

Table 4. Results from (Ryan & Arnold, 1997-1).

In (Tate, 1997) the actual compression ratio for the data from a single AVIRIS image was 3.53. In (Memon, et al., 1994) the entropy of the residual of Cuprite image ranged from 5.48 to 5.61 bits/sample.

3.2 Predictive coding in lossless compression of spectral images

In (Mielikäinen et al., 2002; Mielikäinen et al., 2003) an interband version of predictive coding is presented. Linear prediction is one of the best performing image coding techniques. The least squares estimation approach defines the prediction coefficients from the causal set. An estimate $p'_{x,y,z}$ for the current pixel $p_{x,y,z}$ at location x,y,z is calculated as

$$p'_{x,y,z} = \sum_{k=0}^{O} \sum_{j=0}^{T} \sum_{i=L_{j,k}}^{R_{j,k}} a_{i,j,k} \, p_{x-i,y-j,z-k} \tag{27}$$

where $a_{i,j,k}$ is a prediction coefficient of the pixel at location i,j,k. O is the number of bands and T is the number of rows in the causal set. The $L_{j,k}$ and $R_{j,k}$ are the delimiters in spatial

and spectral dimensions for the causal set. These definitions lead to matrix operations and finally to the causal estimates of the pixel. Since the coefficients $a_{i,j,k}$ are known the estimate of the pixel $p_{x,y,z}$ is defined. The causal set was structured from the spatial and spectral dimensions. In the experiments a small causal set with prediction only from the previous band proved to give the best results. Also the heuristic for prediction was considered, some bands were not predicted but entropy coded without prediction. This enhancement further added the coding performance. The results presented outperformed the results found from the literature.

In Table 5 the average results for AVIRIS images are collected (Mielikäinen et al., 2003). They used the same image data as shown in Table 3. The table contains also reference results from vector quantization (VQ), enhanced principal component analysis with integer wavelets (PCA, see Table 3), the discrete cosine transform (DCT) and finally the results from the methods presented in (Mielikäinen et al., 2003), the prediction and the adaptive prediction (Pred/1, A&P/3).

Image	VQ	PCA	DCT	Pred/1	A&P/3
4 test images	3.06	3.03	2.72	3.14	3.23

Table 5. Results from (Mielikäinen et al., 2003).

A general conclusion from the previous is that the prediction methods work best in spectral image coding. The transform methods are more suitable for lossy compression.

4. Quality in lossy compression

The quality of the lossy compressed/reconstructed image is hard to evaluate. The error measures used in the lossy compression of the spectral images are similar to those used in the compression of the grey-scale or RGB-colour images: the error is evaluated using mean-square-error based quantitative measures like root-mean-square error, signal-to-noise ratio (SNR) or peak-signal-to-noise ratio (PSNR). All of these measures are computed pixelwise and thus, they show limited correlation with the human visual system. For example, the PSNR error remains the same, even though the relative error becomes large. This relative error is important in perceptual measures, since the human visual system notices the intensity variation in grey area better than in dark or bright area (Li et al., 1999).

Qualitative measures are becoming more important, web-based applications like e-commerce will require images with high visual quality.

4.1 Energy-based quality measures

For grey-level images the signal-to-noise ratio (SNR) and the peak-signal-to-noise ratio (PSNR) can be defined as

$$SNR = 10\log_{10}\frac{E^o}{\left|E^o - E^{cr}\right|}, \quad PSNR = 10\log_{10}\frac{N^2 s^2}{\left|E^o - E^{cr}\right|} \tag{28}$$

where s is the peak value of the image, normally $s = 2^8-1 = 255$, E^o is the energy of the original image, E^{cr} is the energy of the compressed/reconstructed image, and N^2 is the number of pixels in the image (Rabbani & Jones, 1991).
These measures have some advantages and some drawbacks. Both of the measures are computed pixel-wise and thus, they show poor correlation with human visual perception. One of the advantages is that these measures can be computed fast: the amount of computations needed is linearly dependent on the size of the spectral image, i.e. $O(n)$, where $n = N*N*M$, and N is the number of pixels in each spatial dimension and M is the number of the spectral bands. Also, any type of images can be used with this measure: greyscale, colour, or spectral images. The PSNR has a constant energy E^o for the images of equal size and thus it provides an absolute measure for the error. For example, if in one pixel image with the resolution of 8 bits, the pixel values are $x_i^o=5$, and $x_i^{cr}=3$, then $PSNR=42.1dB$. If a similar error, two units, is in the range closer to the peak value, like $x_i^o=251$ and $x_i^{cr}=249$, the PSNR remains the same, $PSNR=42.1dB$. Thus the PSNR does not notice the locations of the equal size errors in the intensities of the samples. These locations are important in perceptual measures, since the eyes notice the intensity variation in the grey area better than in the dark or in the bright areas (Li et al., 1999). Despite of this, the PSNR is widely used measure due to the absolute nature. The SNR measure uses energy E^o which is dependent on the values of the image, so the measure is a proportional measure. In the similar case as previously, the SNR measure has different values depending on the range of the pixel values. For example, if $x_i^o=5$, and $x_i^{cr}=3$ in a 8 bit resolution image, then $SNR=8.0dB$. If $x_i^o=251$ and $x_i^{cr}=249$, then $SNR=42.0dB$. For this reason, the SNR values cannot be compared between different sets of images without normalization.

4.2 Content difference-based quality measures

For the spectral image compression a quantitative measure based on the percentage maximum absolute distortion (PMAD) is developed (Ryan & Arnold, 1997-2). The PMAD is measured as a distance between each pixel from the original image and the reconstructed image and it guarantees, that every distance is below $p*100\%$ of the original pixel value. The measure showed predictable behaviour as the compression ratio increased and vice versa. The quality of the compression/reconstruction can be predicted, if the compression ratio is known in advance. The details of PMAD were already described in Section 2.1.

Similarly to PMAD, quality controlled compression methods were developed for near-lossless compression (Aiazzi et al., 2001). The data used was optical data, either pancromatic 2D data or hyperspectral 3D data. Also, psychophysically derived quantization in wavelet based compression has been considered (Ferguson & Allinson, 2002). Their method minimizes distortions and provides smooth perceived degradation for compressed images. Again, colour images were used in the experiments.
The pixel-wise error measures are good for random errors but not for structured or correlated errors (Franti, 1999; Miyahara et al., 1998; Nakauchi et al, 1998). Typical compression artefacts include blockiness, blurring, and jaggedness of the edges and they require spatial consideration, which is based on the original pixel values.
A sliding cube of size 3x3x3 was used to process the spectral image and three components were computed for each pixel: the contrast, the spatial and the spectral structure, and the number of different grey-levels (Kaarna & Parkkinen, 2002). The contrast measures how

each pixel differs from the background. The spatial structure, or the edges, of the image are blurred or jagged in the compression. The number of different grey-levels in a block measures blockiness (Eskicioglu & Fisher, 1995; Franti, 1999; Miyahara et al., 1998). The final measure, the Blockwise Distortion Measure for Multispectral images (BDMM), was calculated using these three components from the original image and from the compressed/reconstructed image. The matching of the BDMM to the visual tests was done with a neural network.

The contrast is a local change in brightness and it is computed using standard deviation (Sonka et al., 1993). The first error component, the contrast error e_c for a block was computed using the difference of the standard deviations for the blocks from the original and the compressed/reconstructed image (Kaarna & Parkkinen, 2002). The spatial and spectral structure is the response to edge detection operations in a block (Sonka et al., 1993). For a three-dimensional 3x3x3 block the three edge detectors G_i, $i=x,y,z$ were filtering operations adopted from Laplacian edge-detectors by modifying the two-dimensional detectors to three-dimensional ones. The second error component, the error e_s in the spatial structure was a sum of all the edge-detection operations normalized with the contrast value of the block (Kaarna & Parkkinen, 2002). The third error component, the quantization error e_q was based on the number of different grey-levels in a block, both from the original image and from the compressed/reconstructed image. The total errors E_c , E_s , and E_q between the original and reconstructed images were received by computing the average values of the blockwise errors e_c , e_s , and e_q over the entire images (Kaarna & Parkkinen, 2002).

The matching between the computed values of the distortion measure BDMM and the visual tests was obtained using a multi-layer perceptron with back-propagation (Kaarna & Parkkinen, 2002). The problem is a curve-fitting problem with three input variables E_c , E_s , and E_q and the goal received from the visual tests V, $BDMM = f(E_c , E_s , E_q , V)$. The function f was modelled by a three-layer neural network with 6 neurons in the hidden layer and one neuron in the output layer. The function f was obtained as the network weights and biases, which are then used to compute the BDMM for all images used in the experiments.

In the experiments three spectral images were used, AISA, AVIRIS, and BRISTOL. Each image was of size 256x256 pixels and they had 32 spectral bands. The spectral range of the AISA (Airborne Imaging Spectrometer for Applications) was from 649 to 747 nm (Aisa, 2006). Our test image contains mainly vegetation. For AVIRIS-image, 32 channels from 1 to 218 by step 7 were selected. Thus, the spectral range is from 370nm to 2450nm. The image is part of one of the Moffet field-images (AVIRIS, 2006). The BRISTOL-image is taken in laboratory conditions from a flower leaf using the visible spectral range from 400 nm to 700 nm (Parraga et al., 1998).

In the experiments three methods were applied to compress the three test images. The three-dimensional wavelet transform with multi-wavelet kernel, the PCA spectral compression and the two-dimensional DCT/JPEG compression were applied. The multispectral images were compressed with several compression ratios and their visual quality was assessed by 18 subjects. After the matching the correlation coefficients for the three different images were computed: for AISA, 0.9911; for AVIRIS, 0.9836; and for BRISTOL, 0.9943. In Fig. 10 we visualize the correlation of the visual grading and the results from the filtering operations after matching.

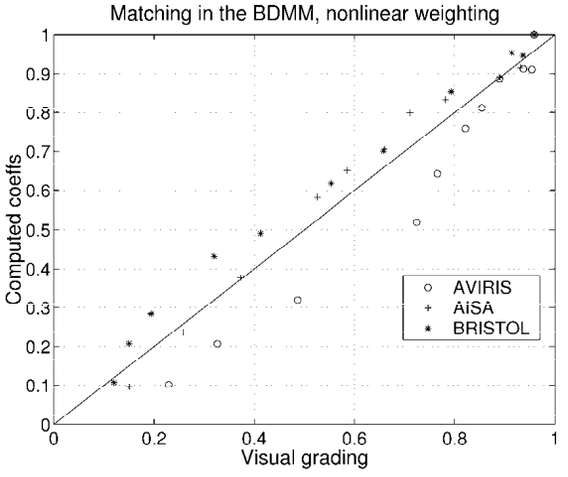

Fig. 10. Visual grading versus filtering operations after matching.

4.3 Spectral–based quality measures

In classification problems, for example in detection of minerals, classification of fields or in environmental monitoring, it is important to find exact matches between two spectra. Thus, comparison of data in vector format is required. Normally, the difference between two vectors is defined using the Euclidean distance (Kaarna et al., 2006).

The Euclidean distance d_e, defined in Eq. 1, measures only the difference in magnitudes between the two spectra and it doesn't observe the shape of spectra. The Euclidean distance is zero for two equal spectra and large values mean large differences in magnitudes of spectra.

Similar vectors have identical magnitudes and directions. The Spectral Similarity Value (SSV) includes these two metrics (Granahan & Sweet, 2001). SSV was defined as

$$SSV = \sqrt{d_e^2 + r_1^2} \tag{29}$$

For Eq. 29, the modified Euclidean distance was defined and the factor *1/n* was inserted under the square root. n is the number of spectral bands in the hyperspectral image. Because a metric, whose large values meant dissimilar vectors, was needed, the coefficient r_1^2 was defined as $r_1 = 1 - r^2$, where r is the correlation between the vectors x and y

$$r^2 = \left(\frac{\frac{1}{n-1}\sum_{i=1}^{n}(x_i - \mu_x)(y_i - \mu_y)}{\sigma_x \sigma_y} \right) \tag{30}$$

where μ_x and μ_y are the mean values for vectors x and y. Respectively, σ_x and σ_x are standard deviations for vectors x and y. The range of r is between zero and one. SSV is zero for identical vectors and larger values mean more dissimilar spectra.

Spectral Angle Mapper (SAM) (Chang, 2000) calculates the angle between two spectra. The SAM only measures the shape of two spectra and it doesn't observe the difference in

magnitudes. The SAM value is zero for similar spectra and larger for more dissimilar spectra. The Spectral Angle Mapper value was defined as

$$SAM=\arccos\left(\frac{\sum_{i=1}^{n} x_i y_i}{\sqrt{\sum_{i=1}^{n} x_i^2}\sqrt{\sum_{i=1}^{n} y_i^2}}\right) \quad (31)$$

In the experiments the Euclidean distance, SSV and SAM were used for spectral matching after the original image was clustered into groups. The vectors of the original image were matched to the cluster centres and the spectral matching was applied also to the vectors of a compressed image. After that the results were compared. In optimum all pixels should have gone to the same clusters in both cases. However, the information loss in the lossy compression normally results in classification inaccuracies, which are lower than 100%. Classification accuracy was used to measure the image quality of a compressed image.
The Euclidian distance performed similarly with the two test images. SSV was more vulnerable than SAM in compression with the image with higher standard deviation. When the image contained larger spatial equi-value areas, the situation was vice versa. The approach of defining the spectral differences was reasonable but it still requires more research.

5. Conclusions

In this section we have collected experiences when different spectral images were compressed in a lossy manner with various methods described in the previous sections.
The following abbreviations are used:

- CL-W: wavelet transform in the spectral reduction followed by clustering,
- CL-P: PCA in the spectral reduction followed by clustering,
- WT-3M: the three-dimensional wavelet transform, Chui-Lian multiwavelets (Chui & Lian, 1996),
- WT-3H: the three-dimensional wavelet transform, Haar wavelet,
- SP-P: PCA in the spectral reduction and SPIHT (Said & Pearlman, 1996) in the spatial dimensions,
- JP2K-P: PCA in the spectral reduction and JPEG2000 (Taubman & Marcellin, 2002) in the spatial dimensions,
- JPG-P: PCA in the spectral reduction and DCT/JPEG (Rabbani & Jones, 1991) in the spatial dimensions,
- SP-O: SPIHT in the spatial dimensions, no spectral reduction,
- JPG-O: DCT/JPEG in the spatial dimensions, no spectral reduction,
- JP2K-O: JPEG2000 in the spatial dimensions, no spectral reduction.

In earlier experiments (Kaarna et al., 2000), it was found, that PCA and wavelets performed best with clustering, and, thus, from the comparisons we leave out the other possible variations.
The last three methods provided trivial solutions to the compression of spectral images. These methods applied SPIHT, DCT/JPEG, or JPEG2000 to the spatial dimensions of the images without any compression in the spectral dimension. Thus, we could get some

indication of the spectral redundancy, and we could also compare the two-dimensional compression methods to each other. The wavelet based compression methods, like the set partitioning in hierarchical trees (SPIHT) and JPEG2000 are effective definitions and implementations of a two-dimensional wavelet compression technique. DCT/JPEG is not of as high quality, but there has been progress also with the discrete cosine transform (Ponomarenko et al., 2005). They have extended the original 8*8 block size to 32*32 block size and carefully considered the quantization of the DCT coefficients.

In spectral image compression one has to consider the noise from the imaging system. The apparent noise is most often modelled as additive noise and there are automatic methods for removing this kind of noise resulting to high quality, noise free images (Ponomarenko et al., 2006). In this case, if the image compression is lossless, one can consider the approach as near-lossless, the loss comes from removing the noise, not any part of the information. If the noise removal should be automatic, then the noise model should well match to the imaging system and the algorithms should be carefully designed and implemented.

In the experiments we had totally 65 images from three data-sets, AISA, AVIRIS and BRISTOL, see section 4.2. Every image was compressed with the methods described above. All the experiments were performed in Matlab-environment.

Comparison to the references in the literature is not straight-forward, since various images and quality measures have been used in different studies. Thus, similar exact CR/PSNR comparison results cannot be presented as are presented for the standard RGB colour images like Lena-image.

In Tables 6 and 7 we give general comments on the compression methods described. The tables contain the summary of our experiments. In the tables a minus sign means that the approach has a bad property, doubled or tripled minus signs mean even worse property value. A plus sign means a positive property value. In Table 7, the compression quality is a combination of the compression ratio and the respective reconstruction quality. This general evaluation is based on the detailed errors included also in the table.

Method	Spectral compression	complexity	Independency of the eimage
SP-O	No	-	+
JPG-O	No	-	+
JP2K-O	No	-	+
CL-P	Yes	- -	-
CL-W	Yes	-	-
SP-P	Yes	- -	-
JPG-P	Yes	- -	-
JP2K-P	Yes	- -	-
WT-3M	Yes	- - -	+
WT-3H	Yes	- -	+

Table 6. Summary of the experiments with different compression methods for spectral images, compression features. - means poor, + means good value of property, multiple symbols mean stronger emphasis.

Method	Compression ratio	Blocking artefacts	Ringing artefacts	Structural errors	Compression quality
SP-O	- -	+	- -	+ + +	+
JPG-O	- - -	- - -	+	- -	-
JP2K-O	- -	+	- -	+ + +	+
CL-P	+ +	- -	+	+ +	+
CL-W	+	- -	+	+ +	-
SP-P	+ + +	+ +	-	+ + +	+ + +
JPG-P	+ +	- -	+	- -	+
JP2K-P	+ + +	+ +	-	+ + +	+ + +
WT-3M	+ +	+	-	+	+ +
WT-3H	+ +	+	- -	+	+

Table 7. Summary from the experiments with different compression methods for spectral images, compression ratio and the quality of compression. - means poor, + means good value of property, multiple symbols mean stronger emphasis.

Currently, the up-to-date system for the lossy compression of the spectral images contains the principal component analysis for the decorrelation of the spectral domain. Then this is followed by a two-dimensional transform for compression the eigenimages. Currently, the wavelet transform is the up-to-date choice for the two-dimensional compression. In the lossless case, the prediction based approaches produce the best coding results.

6. References

Abousleman, G. P.; Gifford, E. & Hunt, B. R. (1994). Enhancement and Compression Techniques for Hyperspectral Data, *Optical Engineering*, Vol. 33, No. 8 (Aug. 1994), pp. 2562—2571.

Abousleman, G. P.; Lam, T. T. & Karam L. J. (2002). Robust Hyperspectral Image Coding with Channel-Optimized Trellis-Coded Quantization, *IEEE Transactions on Geoscience and Remote Sensing*, Vol. 40, No. 4 (Apr. 2002) pp. 820—830.

Abousleman, G. P.; Marcellin, M. W. & B.R. Hunt, B. R. (1995). Compression of Hyperspectral Imagery Using the 3-DCT and Hybrid DPCM/DCT, *IEEE Transactions on Geoscience and Remote Sensing*, Vol. 33, No. 1, (Jan. 1995), pp. 26—34.

Abousleman, G. P.; Marcellin, M. W. & Hunt, B. R (1997). Hyperspectral Image Compression Using Entropy-Constrained Predictive Trellis Coded Quantization, *IEEE Transactions on Image Processing*, Vol. 6, No. 4, (1997) , pp. 566—573.

Adams, M.D. & Kossentini, F. (2000) Reversible integer-to-integer wavelet transforms for image compression: performance evaluation and analysis, *IEEE Transactions on Image Processing*, Vol. 9, No. 6 (June 2000), pp. 1010—1024.

Aiazzi, B.; Alba, P.; Alparone, L. & Baronti, S. (1999). Lossless Compression of Multi/Hyper-Spectral Imagery Based on a 3-D Fuzzy Prediction, *IEEE Transactions on Geoscience and Remote Sensing*, Vol. 37, No. 5 (Sep. 1999), pp. 2287—2294.

Aiazzi, B.; Alparone, L. & Baronti, S. (2001). Near-Lossless Compression of 3-D Optical Data, *IEEE Transactions on Geoscience and Remote Sensing*, Vol. 39, No. 11 (Nov. 2001), pp. 2547—2557.

Aiazzi, B.; Alparone. L. & Baronti, S. (2002). Context Modeling for Near-Lossless Image Coding, *IEEE Signal processing Letters*, Vol. 9, No. 3 (March 2002), pp. 77--80.

Aisa Eagle (2006). AISA Eagle Data Sheet. Specim. http://www.specim.fi. Accessed 27.12.2006.

AVIRIS (2006). AVIRIS Home Page, National Aeronautics and Space Administration, Jet Propulsion Laboratory. http://makalu.jpl.nasa.gov/ aviris.html, accessed Dec. 27, 2006.

Aware (2006). Aware JPEG2000-3D: Compression of volumetric medical image data using JPEG2000-Part 2. http://www.aware.com/products/compression/J2K3D.html. Accessed Dec. 28, 2006.

Bell, T.; Witten, I. H. & Cleary, J. G. (1989). Modeling for data compression, *ACM Computing Surveys*, Vol. 21, No. 4 (Dec. 1989), pp. 557—591.

Berger, T. & Gibson, J. D. (1998). Lossy Source Coding, *IEEE Transactions on Information Theory*, Vol. 44, No. 6 (Oct. 1998), pp. 2693—2723.

Benazza-Benyahia, A.; Pesquet, J.-C. & Hamdi, M. (2001). Lossless Coding for Progressive Archival of Multispectral Images, *IEEE International Conference on Acoustics, Speech, and Signal Processing* (2001), pp. 1817—1820.

Calderbank, A.R.; Daubechies, I.; Sweldens, W. & Yeo, B-L. (1998) Wavelet transforms that map integers to integers, *Applied and Computational Harmonic Analysis*, No. 5 (1998), pp. 332—369.

Chang, C.-I. (2000). An Information-Theoretic Approach to Spectral Variability, Similarity, and Discrimination for Hyperspectral Image Analysis, *IEEE Transactions on Information Theory*, Vol. 46, 2000, pp. 1927—1932.

Chui, C. K. (1992). *An Introduction to Wavelets,* Academic Press, USA, 1992.

Chui, C. K. & Lian, J. (1996) A Study of Orthonormal Multi-wavelets, *Journal of Applied Numerical Mathematics*, Vol. 20 (1996), pp. 273—298.

Cohen, A.; Daubechies, I. & Feauveau, J.-C. (1992). Biorthogonal bases of compactly supported wavelets, *Communications on Pure and Applied Mathematics*, Vol. 45, 1992, pp. 485—560.

Coifman, R. R. & Wickerhauser, M. W. (1992). Entropy-based algorithms for best basis selection, *IEEE Transactions on Information Theory*, Vol. 38, No. 2 (March 1992), pp. 713--718.

Daubechies, I. (1988) Orthonormal bases of compactly supported wavelets, *Communications on Pure and Applied Mathematics*, Vol. 41, No. 7 (Oct. 1988), pp. 909—996.

Daubechies, I. (1992) *Ten Lectures on Wavelet*s, CBMS-NSF, Regional Conference Series in Applied Mathematics, 61, SIAM, USA (1992).

Daubechies, I. (1998) Recent results in wavelet applications, *Journal of Electronic Imaging,* Vol. 7, No. 4 (Oct 1998), pp. 719—724.

DeVore, R. A.; Jawert, B.; Lucier, B. L. (1992). Image compression through wavelet transform coding, *IEEE Transactions on Information Theory*, Vol. 38, No. 2 (Oct. 1992), pp. 719—746.

Donoho, D. L.; Vetterli, M.; DeVore, R. A. & Daubechies I.(1998). Data Compression and Harmonic Analysis, *IEEE Transactions on Information Theory*, Vol. 44, No. 6 (Oct. 1998), pp. 2435—2476.

Dragotti, P. L.; Poggi, G. & Ragozini, R. P. (2000) Compression of hyperspectral images by three-dimensional SPIHT algorithm, *IEEE Transactions on Geoscience and Remote Sensing*, Vol. 38 (2000), pp. 416—428.

EI (2006). IS&T/SPIE Electronic Imaging. http://electronicimaging.org. Acccessed Dec 27, 2006.

Eskicioglu, A. M. & Fisher, P. S. (1995) Image Quality Measures and Their Performance, *IEEE Transactions on Communications*, Vol. 43, No. 12 (1995), pp. 2959—2965.

Ferguson, K. L. & Allinson, M. N. (2002) Psychophysically derived quantization model for efficient DWT coding, *IEE Proceedings -- Visual, Image and Signal processing*, Vol. 149, No. 1 (2002), pp. 51—56.

Fränti, P. (1999) Blockwise distortion measure for statistical and structural errors in digital images, *Signal Processing: Image Communication*, Vol. 13 (1998), pp. 89—98.

Gelli, G. & Poggi, G. (1999). Compression of Multispectral Images by Spectral Classification and Transform Coding, *IEEE Transactions on Image Processing*, Vol. 8, No. 4, (1999) pp. 476—489.

Granahan, J. C. & Sweet, J. N. (2001). An Evaluation of Atmospheric Correction Techniques Using the Spectral Similarity Scale, *Proceedings of the IEEE International Geoscience and Remote Sensing Symposium, IGARSS'01*, Sydney, Australia, 2001, vol. 5, pp. 2022—2024.

Gray, R. M. & Neuhoff, O. L. (1998). Quantization, *IEEE Transactions on Information Theory*, Vol. 44, No. 6 (Oct. 1998), pp. 2325—2383.

Grochowski, E. & Halem, R. D. (2003). Technological impact of magnetic hard disk drives on storage systems. *IBM Systems Journal,* Vol. 42, No. 2 (2003), pp. 338—346.

Hauta-Kasari, M.; Miyazawa, K.; Toyooka, S. & Parkkinen, J. (1999). Spectral Vision System for Measuring Color Images. *The Journal of the Optical Society of America A,* Vol. 16, No. 10, (1999), 2352—2362.

Hughes, G. F. (2002). Computers: wise drives, *IEEE Spectrum,* Vol. 39, No. 8 (Aug. 2002), pp. 37—41.

HYDICE (Hyperspectral Digital Imagery Collection Experiment) (2006). Goodrich Corporation. http://www.oss.goodrich.com. Accessed Dec. 27, 2006.

HyMap Airborne Scanners (2006). Integrated Spectronics. http://www.intspec.com. Accessed Dec. 27, 2006.

Hyvärinen, T.; Herrala, E. & Dall'Ava, A. (1998). Direct Sight Imaging Spectrograph: a Unique Add-on Component Brings Spectral Imaging to Industrial Applications, *Proc. of SPIE Conference on Digital Solid State Cameras: Designs and Applications,* SPIE Vol. 3302 (Apr. 1998), 165—175.

Hyperion (2006). National Aeronautics and Space Administration, Earth Observing-1, Hyperion Instrument. http://eo1.gsfc.nasa.gov. Accessed Dec. 27, 2006.

IGARSS (2006). IEEE International Geoscience and Remote Sensing Symposium. http:// www. grss-ieee.org. Accessed Dec 27, 2006.

Ikonos (2006). Space Imaging. IKONOS earth imaging satellite. http://www.spaceimaging. com. Accessed Dec. 27, 2006.

JPEG2000 (2006). JPEG 2000 3D (Part 10 –JP3D). http://www.jpeg.org/jpeg2000/j2part10.html. Accessed Dec 28., 2006.

Kaarna, A. (2001). Integer PCA and wavelet transforms for multispectral image compression *IEEE International Geoscience and Remote Sensing Symposium, IGARSS'01,* Vol. 4 (July, 2001), pp. 1853—1855.

Kaarna, A. & Parkkinen, J. (1999). Multiwavelets in Spectral Image Compression, *Proc. 11'th Scandinavian Conference on Image Analysis*, Kangerlussuaq, Greenland, June 7--11, 1999, pp. 327—334.

Kaarna A., Parkkinen, J. (2001) Transform Based Lossy Compression of Multispectral Images, *Pattern Analysis & Applications*, Vol. 4, No. 1, 2001, pp. 39—50.

Kaarna, A. & Parkkinen, J. (2002). Quality metric for multispectral image compression, *Journal of the Imaging Society of Japan*, Vol. 41, No. 4 (2002), pp. 379—391.

Kaarna, A.; Toivanen, P. & Keränen, P. (2006). Compression and Classification Methods for Hyperspectral Images, *Pattern Recognition and Image Analysis*, Vol. 16, No. 3 (Sept. 2006), pp. 413—424.

Kaarna, A.; Zemcik, P.; Kälviäinen, H. & Parkkinen, J. (1998). Multispectral image compression, *14th International Conference on Pattern Recognition,* Vol. 2, 16-20 Aug. 1998, Brisbane, Australia, pp. 1264—1267.

Kaarna, A.; Zemcik, P.; Kälviäinen, H. & Parkkinen, J. (2000). Compression of Multispectral Remote Sensing Images Using Clustering and Spectral Reduction, *IEEE Transactions on Geoscience and Remote Sensing*, Vol. 38, No. 2 (March 2000) pp. 1073—1082.

Kamano, A.; Morimoto, M. & Nagura, R. (2001). Multispectral Image Compression using Hierarchical Vector Quantization, *IEEE International Geoscience and Remote Sensing Symposium, IGARSS'2001*, Vol. 4, 9-13, July, Sydney, Australia, pp. 1856—1858.

Karhunen, J. Joutsensalo, J. (1995). Generalizations of Principal Component Analysis, Optimization Problems, and Neural Networks, *Neural Networks*, Vol. 8, N0. 4, 1995, pp. 549—563.

Kerekes, J. P. & Baum, J. E. (2002). Spectral Imaging System Analytical Model for Subpixel Object Detection, *IEEE Transactions on Geoscience and Remote Sensing*, Vol. 40, No. 5 (May 2002), pp. 1088—1101.

Kälviäinen, H.; Kukkonen, S.; Hyvärinen, T. & Parkkinen, J. (1998). Quality Control in Tile Production, *Proc. the SPIE Conference on Intelligent Robots and Computer Vision* XVII, SPIE Vol. 3522 (1998), pp. 355—365.

Landsat (2006). National Aeronautics and Space Administration, Goddard and U.S. Geological Survey. http://landsat.gsfc.nasa.gov. Accessed Dec 27, 2006.

Langdon Jr., G. G. (1984) An introduction to arithmetic coding, *IBM Journal of Research and Developmen*t, Vol. 28, No. 2 (March 1984), pp. 135—149.

Lelewer, D. A. & Hirschberg, D. S. (1987). Data compression, *ACM Computing Surveys*, Vol. 19, No. 3 (Sept. 1987), pp. 261—296.

Lillesand, T. M. & Kiefer, R. W. (2000). *Remote Sensing and Image Interpretation*, John Wiley & Sons, New York, USA.

Li, J.; Chaddha, N. & R.M. Gray, R. M. (1999) Asymptotic Performance of Vector Quantizers with a Perceptual Distortion Measure, *IEEE Transactions on Information Theory*, Vol. 45, No. 4 (1999), pp. 1082—1091.

Mallat, S. (1989) Multiresolution approximation and wavelet orthonormal bases of $L^2(R)$, Transactions of American Mathematical Society, Vol. 315 (Sep. 1989), pp. 69—87.

Mallat, S. (1998) *A Wavelet Tour of Signal Processing*, Academic Press, San Diego, USA, 1998.

MCS (2006). International Symposium on Multispectral Color Science. http://www.multispectral.org. Accessed Dec. 27, 2006.

Memon, N.D.; Sayood, K. & Magliveras, S. S. (1994). Lossless Compression of Multispectral Image Data, *IEEE Transactions on Geoscience and Remote Sensing*, Vol. 32, No. 2, (1994) pp. 282—289.

Mielikäinen, J. (2006). Lossless compression of hyperspectral images using lookup tables, *IEEE Signal Processing Letters,* Vol. 13, No. 3 (March 2006), pp. 157—160.

Mielikäinen, J.; Kaarna, A. & Toivanen, P. (2002) Lossless hyperspectral image compression via linear prediction, *Proceedings of Algorithms and Technologies for Multispectral, Hyperspectral, and Ultraspectral Imagery VIII*, SPIE 4725, Orlando, USA, April 1-5, 2002, pp. 600—608.

Mielikäinen, J.; Toivanen, P. & Kaarna, A. (2003) Linear prediction in lossless compression of hyperspectral images, *Optical Engineering,* Vol. 42, No. 4 (April 2004), pp. 1013—1017.

Mielikäinen, J. & Toivanen P. (2003). Clustered DPCM for the lossless compression of hyperspectral images, *IEEE Transactions on Geoscience and Remote Sensing*, Vol. 41, No. 2 (Dec. 2003), pp. 2943—2946.

Miyahara, M.; Kotani, K. & Algazi, V. R. (1998) Objective Picture Quality Scale (PQS) for Image Coding, *IEEE Transactions on Communications*, Vol. 46, No. 9 (1998), pp. 1215—1226.

Moreiro, F. (2006) STORAGE: Ten-year forecast of storage evolution, Deliverable D12.5, Presto-Space, 2006.

Nakauchi, S.; Hatanaka, S. & Usui, S. (1998) Color gamut mapping by minimizing perceptual differences between images, *Systems and Computers in Japan*, Vol. 29, Issue 10 (1998), pp. 46—56.

Nelson, M. (1996). Data compression with the Burrows-Wheeler transform, *Dr. Dobbs Journal.* http://dogma.net/markn/articles/bwt/bwt.htm, accessed 1.1.2007.

OrbView (2006). Orbimage, OrbView-3 satellite. http://www.orbimage.com. Accessed Dec. 27, 2006.

Parraga, C. A.; Brelstaff, G.; Troscianko, T. & Moorehead, I. R. (1998) . Color and luminance information in natural scenes, *Journal of the Optical Society of America*, JOSA A, Vol. 15, Issue 3 (1998), pp. 563—569.

Poggi, G. & Ragozini, A. R. P. (2002). Tree-structured product-codebook vector quantization, *Signal Processing: Image Communication*, Vol. 16, 2002, pp. 421—430.

Ponomarenko, N.N.; Lukin, V. V.; Egiazarian, K. O. & Astola, J. T. (2005) DCT Based High Quality Image Compression, *Proc. Scandinavian Conference on Image Analysis, Springer Series: Lecture notes in computer science*, Vol. 3540, Joensuu, Finland, June 2005, pp. 1177—1185.

Ponomarenko, N.; Lukin, V.; Zriakhov, M. & A. Kaarna (2006). Preliminary Automatic Analysis of Characteristics of Hypespectral Aviris Images, *International Conference on Mathematical Methods in Electromagnetic Theory*, 26-29 June, 2006, pp. 158—160.

Proakis, J. G. & Manolakis, D. G. (1994). Digital Signal Processing: Principles, Algorithms, and Applications, Macmillan, New York, 1994.

Rabbani, M. & P. W. Jones, P. W. (1991). *Digital Image Compression Techniques*, SPIE - Tutorial Text Series, Volume TT 7, Bellingham, WA, USA.

Rissanen, J. & Langdon Jr., G. G. (1979) Arithmetic coding, *IBM Journal of Research and Development*, Vol. 23, No. 2 (March 1979), pp. 149—162.

Roger, R. E. & Cavenor, M. C. (1996). Lossless compression of AVIRIS images, *IEEE Transactions on Image Processing*, vol. 5, no. 5, (1996) pp. 713—719.

Ryan, M. & Arnold, J. (1997-1) The lossless compression of AVIRIS images by vector quantization, *IEEE Transactions on Geoscience and Remote Sensing*, Vol. 35, No. 3 (May 1997), pp. 546—550.

Ryan, M. J. & Arnold, J. F. (1997-2). Lossy Compression of Hyperspectral Data Using Vector Quantization, *Remote Sensing of Environment*, Vol. 61 (Mar. 1997), pp. 419—436.

Ryan, M. J. & Arnold, J. F. (1998). A Suitable Distortion Measure for the Lossy Compression of Hyperspectral Data, *Proc. the IEEE International Geoscience and Remote Sensing Symposium IGARSS'98*, Vol. 4 (July 1998), pp. 2056—2058.

Said, A. & Perlman, W. A. (1996) A new, fast, and efficient image codec based on set partioning in hierarchical trees, *IEEE Transactions on Circuits and Systems for Video Technology*, Vol. 6, No. 3 (June 1996), pp. 243—250.

Sonka, M.; Hlavac, V. & Boyle, R. (1993) *Image Processing, Analysis and Machine Vision*, Chapman & Hall Computing, Cambridge University Press, England.

Tate, S.R. (1997) Band ordering in lossless compression of multispectral images, *IEEE Transactions on Computers*, Vol. 46, No. 4 (1997), pp. 477—483.

Taubman, D. S. & Marcellin, M. W. (2002). *JPEG2000 Image Compression Fundamentals, Standards and Practice*, Kluwer Academic Publishers, Boston, USA.

Thompson, D. A. & Best, J. S. (2000). The future of magnetic data storage technology, *IBM Journal of Research and Development*, Vol. 44, No. 3 (2000), pp. 311—322.

Toivanen, P.; Lehtinen, A.; Ansamäki, J. and Kälviäinen, H. (1999). Two-Stage Multispectral Image Compression Using the Self-Organizing Map, *Proceedings of the 11th Scandinavian Conference on Image Analysis (SCIA'99)*, Kangerlussuaq, Greenland, June 7-11, 1999, pp. 903—909.

Toivanen P.; Kubasova, O. & Mielikäinen, J. (2005). Correlation-based band ordering heuristics for lossless compression of hyperspectral sounder data. *IEEE Transactions on Geoscience and Remote Sensing Letters*, Vol. 2, No. 1 (Jan. 2005), pp. 50—54.

Vaughn, V.D. & T.S. Wilkinson, T. S (1995). System Considerations for Multispectral Image Compression Designs, *IEEE Signal Processing Magazine*, (Jan 1995), pp. 19—31.

Vetterli, M. & Kovačević, J. (1995) *Wavelets and Subband Coding*, Prentice Hall, USA, 1995.

Vetterli, M., Filter banks allowing perfect reconstruction, *Signal Processing*, Vol. 10, No. 3 (Apr. 1986), pp. 219—244.

Zayed, A.I. (1996). Handbook of function and generalized function transformations, CRC Press, USA, 1996.

Ziv, J. & Lempel, A. (1977). A universal algorithm for sequential data compression, *IEEE Transactions on Information Theory*, Vol. IT-23, No. 3 (May 1977), pp. 337—343.

Ziv, J., Lempel, A. (1978). Compression of individual sequences via variable-rate coding, *IEEE Transactions on Information Theory*, Vol. IT-24, No. 5 (Sept. 1978), pp. 530—536.

Vision Systems: Segmentation and Pattern Recognition

Edited by Goro Obinata and Ashish Dutta

ISBN 978-3-902613-05-9
Hard cover, 536 pages
Publisher I-Tech Education and Publishing
Published online 01, June, 2007
Published in print edition June, 2007

Research in computer vision has exponentially increased in the last two decades due to the availability of cheap cameras and fast processors. This increase has also been accompanied by a blurring of the boundaries between the different applications of vision, making it truly interdisciplinary. In this book we have attempted to put together state-of-the-art research and developments in segmentation and pattern recognition. The first nine chapters on segmentation deal with advanced algorithms and models, and various applications of segmentation in robot path planning, human face tracking, etc. The later chapters are devoted to pattern recognition and covers diverse topics ranging from biological image analysis, remote sensing, text recognition, advanced filter design for data analysis, etc.

InTech Europe
University Campus STeP Ri
Slavka Krautzeka 83/A
51000 Rijeka, Croatia
Phone: +385 (51) 770 447
Fax: +385 (51) 686 166
www.intechopen.com

InTech China
Unit 405, Office Block, Hotel Equatorial Shanghai
No.65, Yan An Road (West), Shanghai, 200040, China
中国上海市延安西路65号上海国际贵都大饭店办公楼405单元
Phone: +86-21-62489820
Fax: +86-21-62489821

IntechOpen